Regulable neural progenitor-specific *Tsc1* loss yields giant cells with organellar dysfunction in a model of tuberous sclerosis complex

June Goto[a], Delia M. Talos[b], Peter Klein[b], Wei Qin[a,1], Yvonne I. Chekaluk[a], Stefanie Anderl[a], Izabela A. Malinowska[a], Alessia Di Nardo[b], Roderick T. Bronson[c], Jennifer A. Chan[d], Harry V. Vinters[e], Steven G. Kernie[f,2], Frances E. Jensen[b], Mustafa Sahin[b], and David J. Kwiatkowski[a,3]

[a]Translational Medicine Division, Department of Medicine, Brigham and Women's Hospital, Boston, MA 02115; [b]The F. M. Kirby Neurobiology Center, Department of Neurology, Children's Hospital Boston, and Program in Neurobiology, Harvard Medical School, Boston, MA 02115; [c]Department of Pathology, Harvard Medical School, Boston, MA 02115; [d]Department of Pathology and Laboratory Medicine, University of Calgary, Calgary, AB, Canada T2N 4N1; [e]Departments of Pathology and Laboratory Medicine and Neurology, University of California Los Angeles Medical Center, Los Angeles, CA 90095; and [f]Department of Pediatrics and Developmental Biology, University of Texas Southwestern Medical Center, Dallas, TX 75390-9133

Tuberous sclerosis complex (TSC) is a multiorgan genetic disease in which brain involvement causes epilepsy, intellectual disability, and autism. The hallmark pathological finding in TSC is the cerebral cortical tuber and its unique constituent, giant cells. However, an animal model that replicates giant cells has not yet been described. Here, we report that mosaic induction of *Tsc1* loss in neural progenitor cells in *Tsc1*cc *Nestin-rtTA*+ *TetOp-cre*+ embryos by doxycycline leads to multiple neurological symptoms, including severe epilepsy and premature death. Strikingly, *Tsc1*-null neural progenitor cells develop into highly enlarged giant cells with enlarged vacuoles. We found that the vacuolated giant cells had multiple signs of organelle dysfunction, including markedly increased mitochondria, aberrant lysosomes, and elevated cellular stress. We found similar vacuolated giant cells in human tuber specimens. Postnatal rapamycin treatment completely reversed these phenotypes and rescued the mutants from epilepsy and premature death, despite prenatal onset of *Tsc1* loss and mTOR complex 1 activation in the developing brain. This TSC brain model provides insights into the pathogenesis and organelle dysfunction of giant cells, as well as epilepsy control in patients with TSC.

Tuberous sclerosis complex (TSC) is an autosomal dominant tumor suppressor gene syndrome characterized by the development of benign tumors in multiple organ systems, with an incidence of ~1:6,000 live births (1, 2). Among the anatomical manifestations of TSC, cortical tubers and subependymal nodules are the hallmark of the disease and occur in about 90% of patients. Multiple neurological features, including epileptic seizures, global developmental delay, autism and autism spectrum disorders, sleep disorders, and other mental health disorders, are clinically devastating issues for many individuals who have TSC and their families (2–6).

TSC cortical tubers exhibit disrupted neuronal laminar architecture, hypomyelination, and the hallmark enlarged, undifferentiated, "balloon-like" giant cells (7, 8), as well as dysmorphic and enlarged neurons, hypertrophic astrocytes, and a variety of reactive cells (9–11). Severe epilepsy is seen in most patients with TSC, and the number and size of tubers correlate with an increased risk for intractable seizures (3, 5), which are associated with poor cognitive outcome (6). Because tubers have been identified in the developing neocortex of patients with TSC as early as 20 wk of gestation (12–14), it is thought that giant cells develop at some point during neural progenitor cell proliferation, neuronal differentiation, and migration. However, the cellular and genetic mechanisms of giant cell development are poorly understood because of the absence of a mouse model that replicates giant cells.

TSC is attributable to inactivating mutations in either *TSC1* or *TSC2* (15, 16), encoding TSC1/Hamartin and TSC2/Tuberin, respectively; both proteins act in a heterodimeric complex (2, 17). The TSC1/TSC2 complex functions as a negative regulator for a small ras family GTPase, Rheb, through GTPase activating protein (GAP) activity of TSC2. GTP-bound active Rheb activates an evolutionarily conserved master cell growth regulator, mTOR serine/threonine kinase complex 1 (mTORC1) (17). Because mTORC1 enhances multiple metabolic and growth-related processes, inactivation of either *TSC1* or *TSC2* leads to robust cell growth and metabolism (17–19), including de novo protein translation as well as lipid biosynthesis (19–21) and mitochondrial biogenesis (22). In addition, activation of mTORC1 inhibits autophagy through various mechanisms (23). Therefore, chronic hyperactivation of mTORC1 induces, whereas administration of mTOR inhibitor rapamycin reverses, the unfolded protein response (UPR)/endoplasmic reticulum (ER) stress (24, 25) and reactive oxygen species (ROS) (25, 26), which lead to insulin resistance (24) and neuronal apoptosis (25). Although there are several mouse models of TSC brain disease, none of them replicates the structural and morphological features of giant cells as found in TSC tubers (27–29).

Here, we report that mosaic loss of *Tsc1* in embryonic neural progenitor cells results in a brain model of TSC with giant cells in the cerebral cortex. These giant cells often develop aberrant lysosomes that progress to vacuoles, which led us to discover this same previously unappreciated feature of TSC tuber giant cells. In addition, these giant cells have a 10-fold increase in mitochondria. Further, this model system permits investigators to choose the timing and extent of cre recombination in neuroprogenitor cells. Thus, this mouse model illuminates the pathogenesis of cortical tubers, providing evidence that biallelic loss of *Tsc1* in neural progenitor cells reproduces giant cells, and provides an important vehicle for additional translational research directed toward prevention of epileptogenesis and other neurological deficits in TSC.

Results

Partial Timed Biallelic Deletion of *Tsc1* in Neural Progenitor Cells. To mimic the timing of cortical tuber development in late-stage TSC fetuses (1, 12–14), we treated pregnant dams whose pups bore doxycycline regulable neural progenitor cell-specific cre alleles and a *Tsc1* homozygous conditional allele (*Tsc1^cc^ Nestin-rtTA-IRES-eGFP^+^ TetOp-cre^+^*) with doxycycline in feed on various gestational days. Doxycycline given on embryonic day 8 (E8) induced cre expression in a small proportion of cells in the thalamus, brainstem, and spinal cord (Fig. 1*A*, first row), whereas doxycycline on E10, when neurogenesis is most active, led to widespread high-level recombination in all brain regions (Fig. 1*A*, second row). We confirmed that nestin-expressing neural progenitor cells expressed the *Nestin-rtTA-IRES-EGFP* allele, including neuroepithelial cells in the basal ventricular zone as well as preplate cells at E10 and E13 (Fig. S1). Doxycycline administration on E13 or E16 [*Tsc1^cc^ Nestin-rtTA^+^ TetOp-cre^+^* (*E13 doxy*) or (*E16 doxy*), respectively] resulted in a restricted pattern of recombination in cortex, hippocampus, and cerebellum (Fig. 1*A*, third and fourth rows), Quantitative copy number analysis of the conditional (*Tsc1^c^*) and null (*Tsc1^−^*) alleles by multiplex ligation-dependent probe assay (MLPA) using newborn brain DNA at P0 confirmed mosaic levels of recombination at the *Tsc1^c^* allele in mice treated at E13 (45%) and E16 (18%) (Fig. S2*A*), demonstrating the regulable expression of cre in this model (30). To examine the timing of loss of *Tsc1* in *Tsc1^cc^ Nestin-rtTA^+^ TetOp-cre^+^* embryos in detail, we performed lacZ staining in the mutant embryo at E16/17 after exposure to doxycycline at E13 (Fig. S2*B*). Strong blue staining reflecting high recombination was seen in the ventricular zone and subventricular zone of cortex and hippocampus, where neural progenitors are enriched. A mosaic pattern of recombination was seen in the developing cortical plate and the CA1 region of the hippocampus, which correlates with the caudal-rostral brain development axis.

Immunoblotting of P0 forebrain lysates demonstrated a decrease in Tsc1 protein levels, along with reduced Tsc2 and mild activation of mTORC1, seen as mildly increased phosphorylated ribosomal protein S6 (pS6) at both Ser235/236 sites and Ser240/244 sites (*P* not significant), as well as negative feedback inhibition of Akt with reduced phospho-Akt (pAkt)-Ser473 levels (Fig. 1*B* and Fig. S2*C*; *P* = 0.028). In comparison with *Tsc1^cc^ Nestin-cre^+^* mice, in which all neural progenitor cells are targeted (31), the level of recombination and the effects on phosphorylation of S6 and inactivation of Akt in *Tsc1^cc^ Nestin-rtTA^+^ TetOp-cre^+^* (*E13 doxy*) mice were milder (Fig. 1*B* and Fig. S2*C*). Analysis of P0 brain sections by immunohistochemistry (IHC) showed that abnormal cells with increased pS6 expression were enriched in the deeper cortical plate of *Tsc1^cc^ Nestin-rtTA^+^ TetOp-cre^+^* (*E13 doxy*) mice (Fig. 1*C*, arrowheads).

The survival of *Tsc1^cc^ Nestin-rtTA^+^ TetOp-cre^+^* mice receiving doxycycline at different embryonic ages correlated well with the extent of *Tsc1* gene recombination (Fig. 1*D* and Fig. S2*A*). E13- and E16-treated mice both had normal development up to postnatal day 21 (P21) and P28, respectively, but then began to die with spontaneous clinical seizures. About half of E8-treated mice died, and several showed severe degeneration of white matter in the cervical spinal cord with Rosenthal fiber-like structures (Fig. S3*A*), likely attributable to recombination in upper spinal cord neurons (Fig. S3*B*). However, because we were interested in a model that might replicate cortical giant cell formation, as seen in TSC cortical tubers, we focused on analysis of the *Tsc1^cc^ Nestin-rtTA^+^ TetOp-cre^+^* (*E13 doxy*) and (*E16 doxy*) mice.

Epileptic Seizures and Neurological Phenotype of *Tsc1^cc^ Nestin-rtTA^+^ TetOp-cre^+^* (*E13 doxy*) Mice. Starting at age P21, *Tsc1^cc^ Nestin-rtTA^+^ TetOp-cre^+^* (*E13 doxy*) mice often showed hyperactive behaviors, such as jumping or running in a circle, and an enhanced startle response. Clinical seizures, characterized by progressive clonus of the limbs, were also observed both spontaneously and in response to physical stimulation, such as handling and noise. To investigate the occurrence of seizures in detail, we performed digital electro-
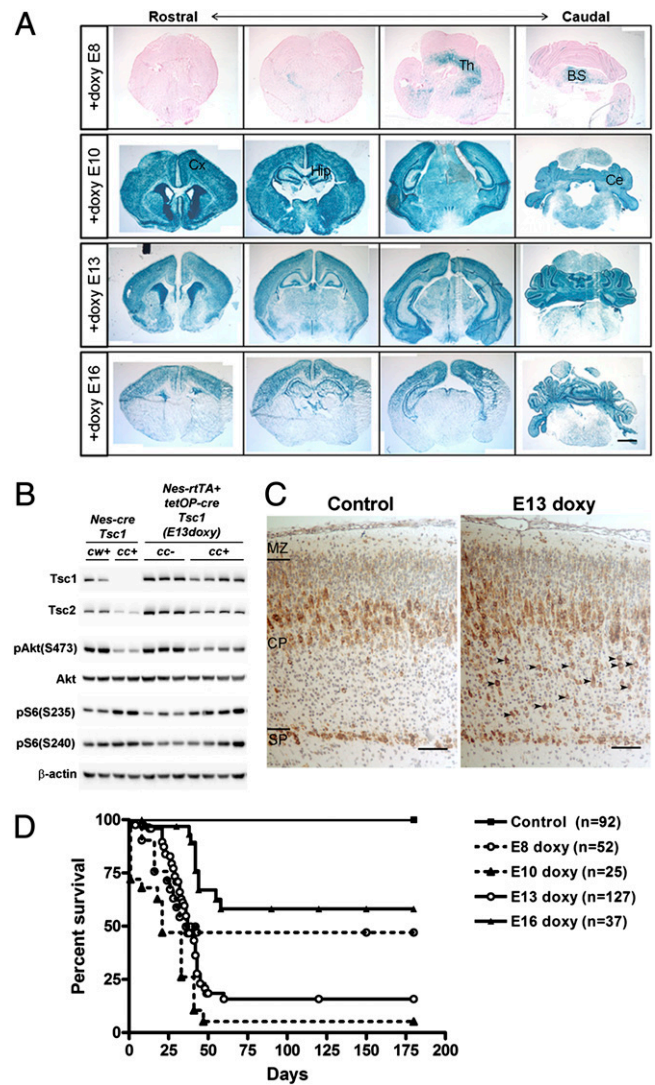
Fig. 1. Mosaic loss of *Tsc1* in doxycycline-treated *Tsc1^cc^ Nes-rtTA^+^ TetOp-cre^+^* mice. (*A*) LacZ staining using rosa26 β-gal allele of P8-P10 *Tsc1^cc^ Nes-rtTA^+^ TetOp-cre^+^* brains treated with doxycycline on different embryonic days (E8–E16). A mosaic pattern of recombination is seen with E13 and E16 doxycycline administration, with recombination mainly in the hippocampus, upper cortex, and cerebellum. (*B*) Immunoblot analysis of P0 brain lysates from *Tsc1^cc^ Nes-rtTA^+^ TetOp-cre^+^* mice (c/c^+^, n = 4) and littermate controls (c/c^−^, n = 3) treated with doxycycline at E13 (*Right*) and from *Tsc1^cc^ Nestin-cre^+^* mice (c/c^+^, n = 2) and littermate controls (c/w^+^, n = 2) (*Left*). *Tsc1^cc^ Nes-rtTA^+^ TetOp-cre^+^* (*E13 doxy*) mice showed partial loss of Tsc1 protein and moderate activation of the mTOR pathway in comparison to *Tsc1^cc^ Nestin-cre^+^* mutants. (*C*) IHC with pS6(Ser235) antibody in P0 brains shows evidence of mTORC1 activation in cortical plate cells (arrowheads) in *Tsc1^cc^ Nes-rtTA^+^ TetOp-cre^+^* (*E13-doxy*) mice. (*D*) Survival of *Tsc1^cc^ Nes-rtTA^+^ TetOp-cre^+^* mice according to day of embryonic doxycycline administration. The control group includes 77 *Tsc1^cc^ Nes-rtTA^+^ TetOp-cre^−^* mice that received doxycycline and 15 *Tsc1^cc^ Nes-rtTA^+^ TetOp-cre^+^* mice that did not receive doxycycline. BS, brainstem; Ce, cerebellum; Cx, cortex; Hip, hippocampus; Th, thalamus. (Scale bars: *A*, 1 mm; *C*, 100 μm.)

encephalography (EEG) and combined video recording. Continuous long-term EEG recordings provided clear electrographic evidence of seizure activity in all mutant mice studied (*n* = 9, ages P25–P42) (Fig. 2 *A–C*). In contrast, all 10 age-matched control mice not carrying the *TetOp-cre* allele showed only the expected normal background EEG activity (Fig. 2*A*, *Upper*). Seizures in the mutants started as high-frequency low-amplitude activity and progressively evolved to high-amplitude sharp wave trains, fol-
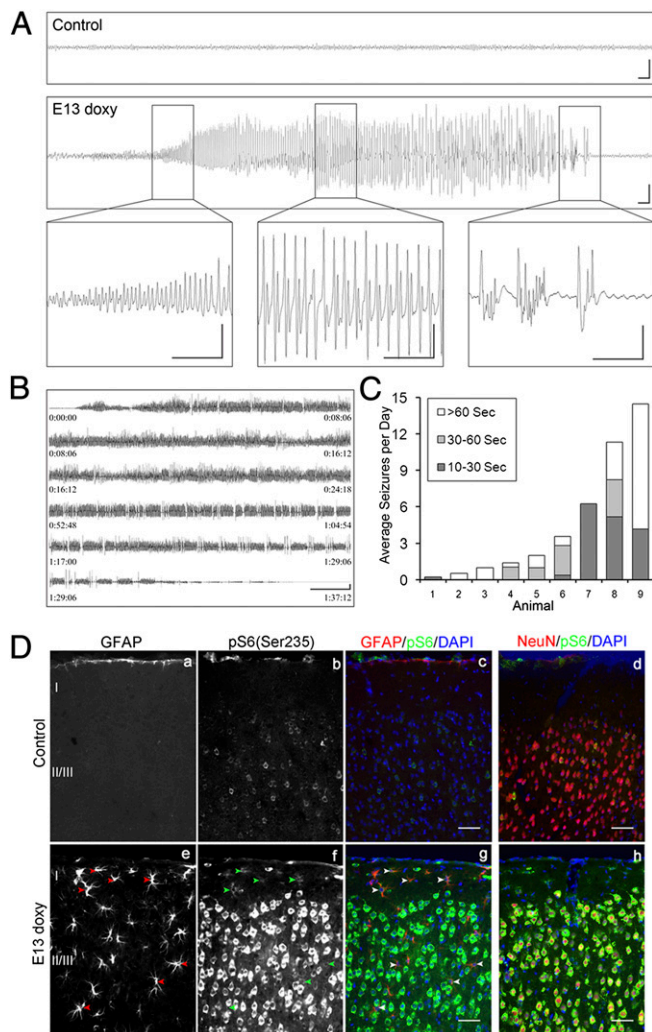
Fig. 2. Spontaneous seizures with neuronal and glial mTORC1 activation in *Tsc1^cc Nes-rtTA^+ TetOp-cre^+* (*E13 doxy*) mice. (*A*) Cortical epidural EEG monitoring of P30 control mice (*Upper*) and *Tsc1^cc Nes-rtTA^+ TetOp-cre^+* (*E13 doxy*) mice (*Lower*), the latter during a seizure. (*Insets*) Onset of seizure activity (*Left*), progression to a period of sharp wave trains (*Center*), and then reduction with a period of postictal slowing (*Right*). (Scale bars: 1 s, 500 μV.) (*B*) Series of near-constant epileptiform discharges recorded in a mutant, leading to the death of this mouse. (Scale bar: 30 s, 500 μV.) (*C*) Average number of seizures per day in nine mutant mice. Shading indicates the duration of the observed seizures in untreated (columns 3, 5, 6, and 9) and vehicle-treated (columns 1, 2, 4, 7, and 8) mutants. (*D*) Immunofluorescence analysis of cortical sections of P55 mutant mice shows an increase in pS6 (Ser235) (*b–d* and *f–h*) in both neurons (*d* and *h*) and astrocytes (*a, c, e,* and *g,* arrowheads). (Scale bars: 50 μm.)

lowed by a reduction in EEG amplitude and postictal slowing, lasting 10–15 s and 1–2 min in most cases (Fig. 2*A, Lower, Insets*). All seizures appeared to be generalized, based on bilateral neocortical recordings. Video recordings indicated that mice typically displayed behavioral arrest, followed by progressive clonus of the limbs and subsequent tonic extension of the trunk and limbs during seizures. In addition, some mice showed a milder seizure type, consisting of chaotic running around the recording chamber. Both behavioral seizure types were accompanied by similar electrographic discharges.

Analysis of EEG recordings at weekly intervals from 4–6 wk of age demonstrated that seizure frequency and duration tended to become more severe with age, because 6 of 10 paired weekly recordings were more severe at the later time point. Severe ter-

minal seizures consisting of near-continuous epileptiform discharges lasting over an hour were recorded in two mice (Fig. 2*B*). The seizure frequency (number of seizures per day) and seizure duration varied greatly among individual mice (Fig. 2*C*). However, electrographic abnormalities were much more severe than what we had previously observed in a neuronal model of TSC (28).

Histological analysis of brains from the *Tsc1^cc Nestin-rtTA^+ TetOp-cre^+* (*E13 doxy*) mice with severe epilepsy demonstrated that hyperactivation of mTORC1 (assessed by pS6 expression) was prominent in both neurons (Fig. 2*D, h*) and enlarged astrocytes (Fig. 2*D, g,* arrowheads). These findings indicate that loss of *Tsc1* in nestin-positive neural progenitor cells leads to generation of both neuronal and glial cells with activation of mTORC1 and suggests that both cell types may contribute to the seizure severity and premature mortality of these mice.

Neuronal Dendritic Abnormalities, ER Stress, and Inflammatory Responses in the Brains of *Tsc1^cc Nestin-rtTA^+ TetOp-cre^+* (*E13 doxy*) Mice. By 6 wk of age, the mutant mice developed progressively severe macrocephaly (Fig. S4 *A–C*) and hyperactivation of mTORC1 (Fig. S4 *F–G*) and down-regulation of mTORC2, as assessed by reduced expression of both total and phospho-PKCα (32, 33) (Fig. S4*G*). Dysmorphic cortical neurons with significant enlargement of both the neuronal soma (20–40 μm in diameter) and nucleus (15–28 μm in diameter) (Fig. S4*A, j,* black arrows, and *D*) were seen, meeting established pathological criteria for this designation (34), as well as ectopic cells in the striatum oriens of the hippocampus (Fig. S4*A, i,* arrowheads, and *E*).

To examine the dendritic architecture of *Tsc1*-null neurons in vivo, we performed Golgi staining. Pyramidal cells in layers V and VI of cerebral cortex of mutant mice developed abnormally complex basal dendrites (Fig. 3*A*). Sholl analysis highlighted significantly increased complexity and total length in layer V and VI pyramidal neurons (Fig. 3*B*). Dendritic abnormalities were more prevalent in neurons that demonstrated aberrant orientation of the apical dendrite (Fig. 3*A, Right*). Polarity defects of *Tsc2*-deficient neurons in cortical cell migration were previously observed in organotypic brain slices (35) and with neuron-specific *Tsc1* deletion (28). The abnormal dendritic arbors seen here are similar to those seen in a *Pten*-deletion brain model with seizures (36, 37). Therefore, these data suggest that neural cell polarity, as well as dendritic complexity, is controlled by proper regulation of mTORC1 and mTORC2 activities.

Cultured *Tsc2*-deficient cells, tuber giant cells, and brain lysates from neuronal *Tsc1* KO mice have shown hyperactivation of mTORC1 and evidence of an enhanced UPR/ER stress attributable to overload of the ER with de novo translated protein (24, 25). In this model, we found hyperactivation of mTORC1 and elevated phospho-eIF2α(Ser52) levels in P30 brain lysates of mutants (Fig. 3*C*). Phospho-eIF2α(Ser52) is known to inhibit the translation initiation factor eIF2B (38), downstream of the PERK and PKR kinases that are activated in response to multiple types of cellular stress, including ER stress, oxidative stress, and viral infections (39, 40). We found all three branches of the ER stress pathway, using the markers *ATF4*, *CHOP*, and a spliced variant of *XBP1* (*XBP1-s*), to be increased at the mRNA level in the hippocampus of symptomatic mutants by real-time quantitative PCR (qPCR; n = 6) (Fig. 3*D*). In addition, *SerpinA3* and *Sparc*, genes involved in inflammation and highly expressed in cortical tuber specimens (41), were significantly increased in expression in the mutant mice. Also, similar to tuber pathology (2, 11), increased GFAP and reduced myelin basic protein (MBP) in brain lysates from *Tsc1^cc Nestin-rtTA^+ TetOp-cre^+* (*E13 doxy*) mice were observed (Fig. 3*C*). Thus, these findings indicate that *Tsc1*-null brain cells have polarity and dendritic morphology defects, as well as ER stress, likely contributing to the development of tuber-like pathology with increased astrocytes and hypomyelination in the mutant brain.

Development of Highly Enlarged Vacuolated Giant Cells in *Tsc1^cc Nestin-rtTA^+ TetOp-cre^+* (*E13 doxy/E16 doxy*) Mice. Intriguingly, we found that by 4–6 mo of age, both *Tsc1^cc Nestin-rtTA^+ TetOp-*
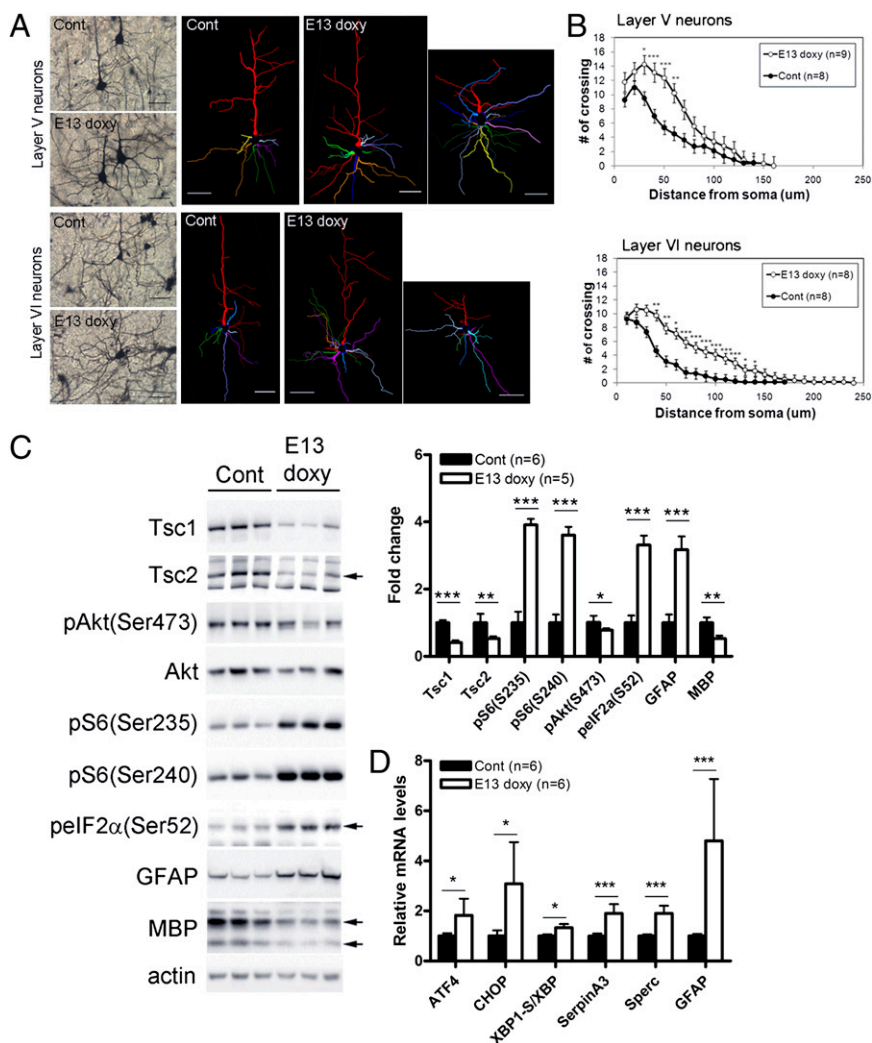
Fig. 3. Dendritic abnormalities, ER stress, and inflammatory response seen in the brains of $Tsc1^{cc}$ $Nes\text{-}rtTA^+$ $TetOp\text{-}cre^+$ (E13 doxy) mice. (A and B) Dendritic morphology of pyramidal neurons in layers V and VI of mutant mice at P30 by Golgi staining and Sholl analysis. (C) Immunoblotting showing a decrease in Tsc1 and Tsc2 expression with mTORC1 activation, a stress response (increased phospho-eIF2αSer52), astrogliosis (increased GFAP), and hypomyelination (MBP) in P30 mutants (n = 3). (D) Real-time qPCR analysis using hippocampal RNAs of six symptomatic mutants at P30. Data have been normalized to 36b4 mRNA levels. Levels of the ER stress markers (ATF4 and CHOP) and inflammatory response genes seen in cortical tubers (SerpinA3 and Sperc) are significantly increased in the mutants. Cont, control. *$P < 0.05$; **$P < 0.01$; ***$P < 0.001$. (Scale bars: A, 50 μm.)

cre^+ (E13 doxy) and $Tsc1^{cc}$ $Nestin\text{-}rtTA^+$ $TetOp\text{-}cre^+$ (E16 doxy) mutants demonstrated highly enlarged cells in radial columns extending from layer VI to layer II/III (Fig. 4A; n = 4). Most of these cells were dysmorphic neurons, as described above. However, some of these cells had TSC giant cell characteristics, including cell diameter >40 μm (Fig. 4B), and opalescent glassy eosinophilic cytoplasm with multiple neural marker expression (Fig. 5). In addition, we observed that some giant cells contained multiple vacuoles in their cytoplasm (Figs. 4 and 5 and Fig. S5). Vacuoles were of variable size and number but commonly formed extensive collections in distended cell bodies (Fig. S5A). We also occasionally observed binucleated cells (Fig. S5B) similar to giant cells in cortical tubers, implying abnormalities in cell division. Fifteen percent of pS6$^+$ cells in the $Tsc1^{cc}$ $Nestin\text{-}rtTA^+$ $TetOp\text{-}cre^+$ (E13 doxy) mouse brains met size criteria for giant cells (2, 34) (Fig. 4B). Vacuolated cells were bigger, on average, than nonvacuolated cells, but 3% of nonvacuolated pS6$^+$ cells had diameters over 40 μm (Fig. 4B). Giant cells were found widely distributed in the cortex and hippocampus in the mutants, often in clusters surrounded by normal tissue (Fig. 4C), similar to the focal pathology of cortical tubers in patients with TSC.

By immunostaining, the giant cells showed strong pS6 positivity, indicating hyperactivity of mTORC1 attributable to loss of Tsc1 (Fig. 4D, arrows). Notably, we found similar vacuoles in giant cells in 24 of 29 cortical tuber specimens from patients with TSC. Both vacuolated giant cells and typical eosinophilic pale giant cells were seen in a tuber resected from an 8-y-old patient with TSC for seizure control (Fig. 4E). The majority of vacuolated and nonvacuolated giant cells in human specimens showed pS6 positivity by IHC, consistent with mTORC1 activation secondary to complete loss of either TSC1 or TSC2. Therefore, $Tsc1^{cc}$ $Nestin\text{-}rtTA^+$ $TetOp\text{-}cre^+$ (E13 doxy/E16doxy) mice replicate a previously underappreciated feature of the neuropathology of TSC cortical tuber cells.

Immunostaining studies showed that the giant cells seen in this model shared multiple features with cortical tuber giant cells. First, they expressed a low level of Tsc2 in comparison to adjacent smaller neurons and neurons in control brains because of loss of Tsc1 protein and destabilization of Tsc2 (Fig. 5A, h). Second, they expressed the neural progenitor marker nestin (Fig. 5A, i), along with neuronal markers, such as SMI311 (Fig. 5A, j), and somewhat weaker expression of NeuN (Fig. 5A, k) and HuD (Fig. 5A, l), in comparison to normal neurons. Third, these cells accumulated pathological levels of axonal proteins highlighted by the Bielschowsky stain (Fig. 5A, m). Fourth, markedly enlarged astrocyte-derived giant cells were also seen in this model (Fig. 5A, n). Finally, we found that nestin-expressing giant cells also expressed receptor subunit profiles for the excitatory neurotransmitter glutamate, such as NR2D and GluR4, which are commonly seen in nonneuronal cortical cells and have been shown to be highly expressed in human cortical tuber giant cells (9). Thus, these data provide evidence that Tsc1-null neural progenitor cells develop into giant cells with undifferentiated neural expression pattern. Giant cells were seen as early as 4 mo of age but were not seen at P60 (n = 3), suggesting that they require both embryonic Tsc1 loss in neural progenitor cells and extensive development.
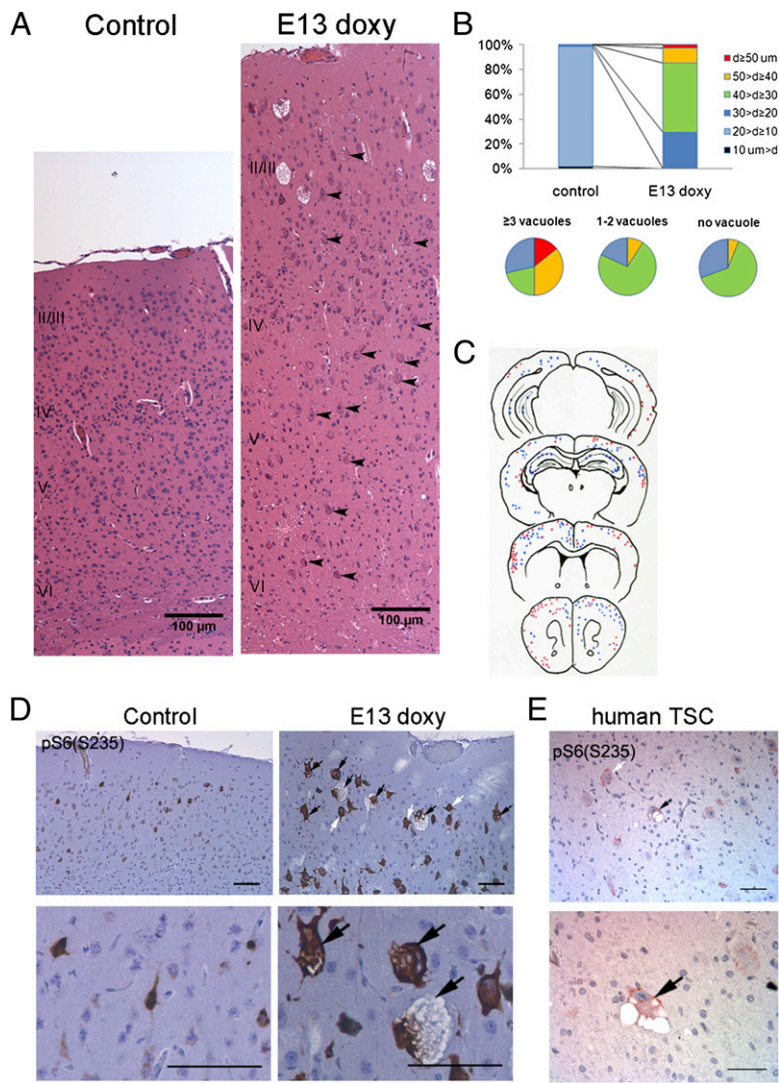
Fig. 4. Brain pathology and vacuolated giant cells in *Tsc1^cc Nes-rtTA^+ TetOP-cre^+* (*E13 doxy*) mice. (*A*) Vacuolated neurons in layers I–III and giant cells in a radial column (arrowheads) in the cortex (*Right*). (*B*) Cell size analysis. The diameter (d) of pS6^+ cortical cells was measured (*n* = 70 cells, 2 animals). Note that in controls, 99% of pS6^+ cells have a diameter <20 μm, whereas the converse is true in mutants. The distribution of cell size according to the number of vacuoles is shown at the bottom. (*C*) Location of giant cells (*d* > 40 μm) in a mutant brain. Red indicates clusters of giant cells with vacuoles, and blue indicates clusters of nonvacuolated giant cells. (*D*) Brain sections of control (*Left*) and *Tsc1^cc Nes-rtTA^+ TetOp-cre^+* (*E13 doxy*) mutant (*Right*) mice at the age of 6 mo show enlarged balloon-like giant cells (white arrows), and giant cells with intracellular vacuoles (black arrows) by IHC using pS6(Ser235). (*E*) Giant cells with (black arrows) and without (white arrow) vacuoles found in cortical tubers of pediatric patients with TSC by IHC using pS6(Ser235) antibody. (Scale bars: *A*, 100 μm; *D* and *E*, 50 μm.)

Immature Lysosomes, Mitochondria Expansion, and Organelle Degeneration and Ultrastructural Analysis of Vacuolated Giant Cells. To characterize the vacuoles seen in giant cells, we performed EM on brain sections from 6-mo-old *Tsc1^cc Nestin-rtTA^+ TetOp-cre^+* (*E16 doxy*) mice. By means of EM, we observed protein-like material of weak opacity in the vacuoles in the giant cells (Fig. 6*A*, *c*, asterisk). The lining membranes of the vacuoles were single-walled structures, which were different from lipid droplets, or typical autolysosomes or autophagosomes. The smaller vacuoles appeared to contain organelles undergoing degradation, including mitochondria, fragmented ER, endosome, and ribosome (Fig. 6*A*, *c*, arrowheads), as well as small vesicles (Fig. 6*A*, *d*, arrows). Immuno-EM using anti-LAMP1 (lysosome marker) (Fig. S6*A*, *a*) and anti-Grp78 (ER marker) (Fig. S6*A*, *b*) revealed that the vacuoles were derived from immature lysosomes enclosing fragmented ER and did not consist of ER membrane itself. Endosomes were found inside the vacuoles, being seen as small round membrane structures positive for either Rab7 (late endosome marker) (Fig. S6*A*, *c*) or EEA1 (early endosome marker) (Fig. S6*A*, *d*). The vacuoles were negative for anti-LC3 antibody in immuno-EM (Fig. S6*A*, *e*) and different from typical LC3^+ double-walled autophagosomes (Fig. S6*A*, *f*). Together, these studies provide evidence that the vacuoles are not derived from the classic autophagy pathway but are more likely aberrant defective lysosomes.

EM studies also demonstrated that both mitochondrial number (Fig. 6*B* and *C*) and fragmented ER (Fig. S6*B*) were dra-

matically increased in vacuolated giant cells in comparison to normal neurons from control mice. The density of mitochondria in giant cells with limited vacuoles (<25% of total cytoplasmic area; 1.00 ± 0.32 per μm^2) was significantly higher than in normal neurons from control mice (0.42 ± 0.06 per μm^2) (Fig. 6*C*, per area). In addition, because giant cells have a 4.1-fold larger cell size compared with controls (Fig. 4), the total number of mitochondria per cell was about 9.7-fold that of normal cells (Fig. 6*C*, per cell). Real-time qPCR analysis of mtDNA compared with genomic DNA (gDNA) also documented an increased level of mtDNA in brain DNA samples from *Tsc1^cc Nestin-rtTA^+ TetOp-cre^+* (*E16 doxy*) mice (Fig. 6*D*). Combining the elevated (2.1-fold) mtDNA/gDNA ratio in total brain DNA (Fig. 6*D*, per brain) with the fraction of cells undergoing recombination in these same samples ($13.2 \pm 0.02\%$ by MLPA) (Fig. S2*A*) leads to a similar estimate that giant cells contain over ninefold more mtDNA in comparison to controls (Fig. 6*D*, per cell). Therefore, this animal model provides evidence of multiorganelle dysfunction in *Tsc1*-null giant cells: defective lysosomes, fragmented and stressed ER, and increased mitochondria.

Rapamycin Treatment Extends Survival of *Tsc1^cc Nestin-rtTA^+ TetOp-cre^+* (*E13 doxy*) Mice, Preventing Epileptic Seizures and Other Pathological Features. Interestingly, postnatal rapamycin treatment beginning at P8 dramatically and significantly extended the survival of *Tsc1^cc Nestin-rtTA^+ TetOp-cre^+* (*E13 doxy*) mice (Fig. 7*A*), despite the prenatal onset of mTORC1 activation (Fig. 1 *B* and *C* and
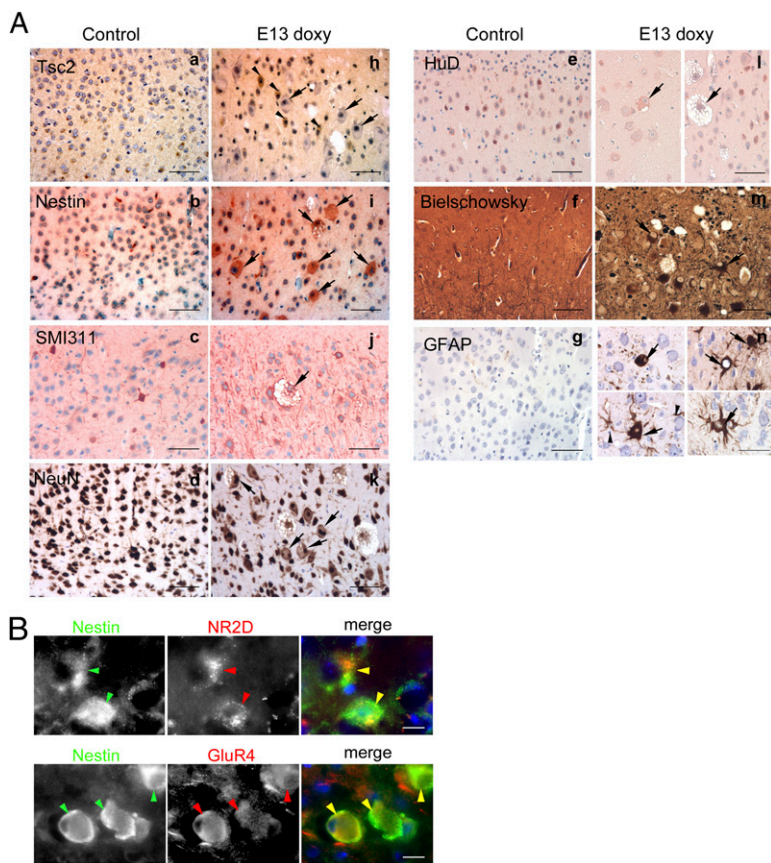
Fig. 5. Expression studies showing the giant cells seen in *Tsc1^cc Nes-rtTA^+ TetOp-cre^+* (*E13 doxy*) mutant mice express multiple neural markers. (*A*) Brain sections of *Tsc1^cc Nes-rtTA^+ TetOp-cre^+* (*E13 doxy*) mutant at the age of 6 mo show enlarged giant cells (black arrows) that lack expression of Tsc2 (*a* and *h*), express high levels of nestin (*b* and *i*) and neurofilaments (SMI311; *c* and *j*), weakly express NeuN (*d* and *k*), more weakly express HuD compared with normal neurons (*e* and *l*), and also contain neurofibrillary tangles (Bielschowsky stain; *f* and *m*). Markedly enlarged GFAP^+ giant cells are also seen (black arrows, *g* and *n*). Note that neurons expressing Tsc2 are of normal size (black arrowheads in *h*). (Scale bars: 50 μm.) (*B*) Colocalization of nestin and NR2D (*Upper*) and nestin and GluR4 (*Lower*) in giant cells. (Scale bars: 20 μm.)

Figs. S1 and S2*B*). However, continuing rapamycin treatment was required, because within 2 wk after rapamycin withdrawal at the age of P55, the mutants developed neurological symptoms and died, suggesting rapid recurrence of major neuropathological abnormalities when rapamycin is discontinued (Fig. 7*A*).

Rapamycin also suppressed seizure activity. Because rapamycin treatment led to a growth delay (P30 male: control, 17.2 ± 1.6 g; control + rapamycin, 10.6 ± 0.9 g; mutant, 17.4 ± 2.5 g; mutant + rapamycin, 11.5 ± 2.1 g; P30 female: control, 13.6 ± 1.9 g; control + rapamycin, 10.0 ± 1.5 g; mutant, 14.2 ± 1.8 g; mutant + rapamycin, 11.5 ± 1.8 g; $n > 5$; $P < 0.001$), electrode placement and EEG recording were performed at a later age in rapamycin-treated mice than in untreated or vehicle-treated mutants (P44–P58 in rapamycin-treated vs. P25–P42 in other). Three consecutive weekly EEG recording sessions demonstrated that spontaneous epileptic seizures were completely absent in rapamycin-treated mutant mice ($n = 4$), in contrast to severe epilepsy detected in vehicle-treated mutants (Fig. 2*C*; $n = 5$). MLPA analysis at the *Tsc1^c* allele in brain DNA samples after EEG recording confirmed significant recombination in all rapamycin-treated mutants that were recorded (recombination: average, 46%; range: 27–56%; $n = 4$).

In addition to clinical benefit in survival and epilepsy control, brain enlargement (Fig. 7*B*) as well as cortical cell enlargement (Fig. 7*C*) was corrected by postnatal rapamycin therapy. Hyperactivation of mTORC1 (increased pS6 levels; Fig. 7*D*), astrogliosis (increased GFAP levels; Fig. 7*D* and *E*), and augmented stress response [increased peIF2α(Ser52) levels; Fig. 7*D*] were also all reversed by rapamycin. qPCR analysis of hippocampal RNA showed normal levels of ER stress (*ATF4*, *CHOP*, and *XBP1-s*) and inflammatory markers (*SerpinA3* and *Sparc*) in the rapamycin-treated mutants (Fig. 7*F*). In addition, the polarity defects seen in apical dendrite orientation was partially rescued by rapamycin treatment, although dendritic arbor abnormalities were not improved and may have worsened to a small extent in

the treated mutants (Fig. S7). Therefore, although recombination is induced at E13 in this model, brain abnormalities responsible for epileptic seizures and many aspects of phenotype are completely reversed by treatment initiated at P8.

Discussion

Refractory epilepsy, intellectual disability, autism spectrum disorder, hyperactivity, and sleep disturbance are common problems in patients with TSC and have a major and ongoing impact on both the patients themselves and their families (2, 3, 6). However, genetic and cellular mechanisms of cortical tuber and giant cell development have been uncertain, partially because of the lack of an authentic animal model (2). In this study, we provide evidence that mosaic biallelic loss of *Tsc1* in neural progenitor cells is sufficient for progressive development of giant cells and focal brain lesions in TSC. We show in a mouse model that bona fide giant cells are derived from nestin-positive *Tsc1*-null neural progenitor cells. In addition, this model highlighted a previously unappreciated cellular feature of giant cells in tubers. A proportion of giant cells in older *Tsc1^cc Nestin-rtTA^+ TetOp-cre^+* (*E13/E16 doxy*) mice had extensive vacuoles, a feature seen in 24 of 29 TSC cortical tuber specimens evaluated in this study. In ultrastructural studies of the vacuoles in this model, we found that vacuoles were positive for LAMP-1, although they did not have typical electron-dense lysosomal characteristics. Recently mTORC1 has been shown to reside on endosome/lysosome membranes (42, 43) and to regulate membrane formation of lysosomes (44). Together with the previous findings that mTORC1 has a critical function in autophagy and lysosome formation (23, 44), these observations suggest consideration of a new therapeutic approach for TSC neurologic manifestations, that of enhancing lysosome-dependent protein degradation. Although further investigation is warranted, our findings suggest that the vacuoles formed as the result of an aberrant attempt to degrade excess proteins and organelles, given the role of mTOR
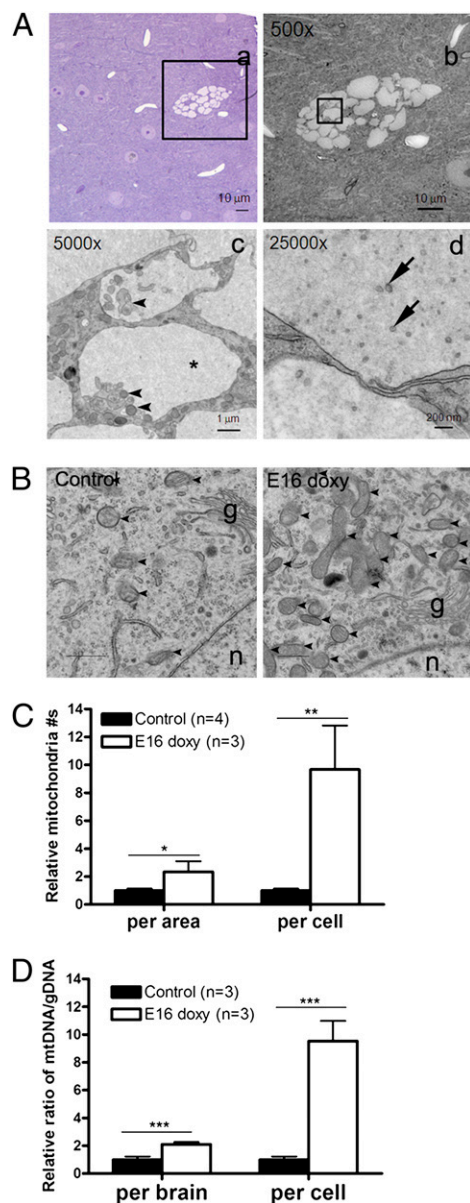
Fig. 6. Ultrastructural analysis of giant cells in *Tsc1^cc Nes-rtTA^+ TetOp-cre^+* (*E16 doxy*) mice. (*A*) Highly vacuolated neurons seen in bright field (*a*) and electron (*b–d*) micrographs. *Insets* in *a* and *b* identify the area enlarged in the next panel. Single-walled vacuoles filled with protein-like material (asterisk), portion of ER membranes and endosomal membranes (arrowheads), and small vesicles (arrows) are shown. (*B*) Increased mitochondria in giant cells with small vacuoles in *Tsc1^cc Nes-rtTA^+ TetOp-cre^+* (*E16 doxy*) giant cells. Mitochondria (arrowheads), the Golgi apparatus (g), and the nucleus (n) are shown. (*C*) Relative mitochondrial density (per area) and contents (per cell) are increased in giant cells in mutants, calculated by considering the 4.1-fold increase in mutant cell volume. (*D*) Quantitative analysis of brain mtDNA content in *Tsc1^cc Nes-rtTA^+ TetOp-cre^+* (*E16 doxy*) mice by real-time PCR, using four mtDNA primer sets in comparison to gDNA primer sets. The relative mtDNA content per *Tsc1*-null cell was calculated considering the 13% level of recombination in *Tsc1* seen in these same samples by MLPA. *$P < 0.05$; **$P < 0.01$; ***$P < 0.001$. Scale bars are indicated in *A*, *a–d*.

signaling in de novo protein synthesis (21), mitochondrial biogenesis (22), and regulation of autophagy. Indeed, we found a 10-fold increase in mitochondrial content of *Tsc1*-null giant cells at 6 mo of age, which progressively increased after birth. This markedly increased mitochondrial content may lead to ROS production as previously observed in *Tsc2*-null cells (22, 25, 26). In addition, we observed fragmented rough ER both in cytoplasm and inside small vacuoles in giant cells, which may be induced by chronic mTORC1 activation and ER stress as the result of an overload of misfolded proteins (24, 25). Interestingly, RNA preparations from the mutant mice also demonstrated the occurrence of an inflammatory response with increased *SerpinA3* and *Sparc* expression, features also seen in TSC cortical tubers (41). Increased *ATF4*, *CHOP*, and *XBP1-s* mRNA levels implicate activation of the UPR, indicating that the giant cells undergo multiple cellular organelle dysfunction attributable to loss of *Tsc1* in brain. These findings enable further development of potential new therapies for TSC, including ER chaperones, ROS scavengers, protein synthesis inhibitors, and protein degradation enhancers.

The limited extent of recombination and long-term survival of these mice has enabled insight into the long-term clinical effects of embryonic loss of *Tsc1* in neuroprogenitor cells. Previously, neuron-specific (28) and radial glia-specific (29) TSC brain models were shown to develop ectopic dysplastic neurons but died after weaning with poor weight gain attributable to extensive levels of recombination. In contrast, nearly all *Tsc1^cc Nestin-rtTA^+ TetOp-cre^+* (*E13 doxy/E16 doxy*) mice developed normally through weaning and then later displayed hyperactive behavior and an enhanced startle response, as is often seen in patients who have TSC. Starting at age P25 or earlier, they also showed consistent onset of severe and malignant epilepsy that progressed to a terminal phase in the majority of mice. This clinical course is quite similar to that seen in a significant fraction of patients with TSC, in whom severe intractable epilepsy causes major morbidity (2, 3, 6). We did observe some variation in the extent of recombination in *Tsc1* as assessed by MLPA and in Tsc1 protein levels (Fig. 7*D*, asterisk) among the mutant mice, likely reflecting variation in the proportion of neural cells with recombination of *Tsc1*, similar to the phenotypic variance of patients with TSC. In the astrocyte-specific Tsc1 brain model (29), there are reduced levels of glutamate transporters (45), and a potential antiepileptic drug (ceftriaxone) has been identified (46). Therefore, a series of therapeutic trials, including antiepileptic drugs, ketogenic dietary therapy, and other potential compounds targeting protein degradation and UPR in this mosaic neuroprogenitor TSC model, will be important future studies.

Pathologically, the mutant mice displayed several features seen in cortical tubers, consistent with the concept that the entire brain has been converted at a mosaic level to the equivalent of a TSC tuber (7, 11, 47, 48). The mutant mice developed giant cells expressing neuroprogenitor markers with enlarged clear cytoplasm and nucleus. Cells with a diameter >40 μm were classified here as giant cells, according to the classification of balloon cells in focal cortical dysplasia (34), but were seen only in mice aged 4 mo or older. Interestingly, this extended developmental period required for giant cell development in this model is similar to what is seen in the fetus with TSC. Focal brain lesions have been noted in fetuses with TSC as early as 19–20 wk of gestation, but they lack balloon-like giant cells (13, 14). Instead, giant cells have been observed in the brain of the fetus with TSC to some extent at 24 wk of gestation and more robustly at 30 wk of gestation (12). Therefore, we propose that in both humans and mice, there is a requirement for several months of progressive growth for *Tsc1*-null (or *Tsc2*-null) neural progenitor cells to develop into balloon-like giant cells. Focal tuber-like brain lesions were recently reported in an in utero electroporation model using the same *Tsc1^c* allele used here to achieve complete loss of Tsc1 (49). Although focal lesions were seen with ectopic enlarged neurons, the neurons did not reach giant cell proportions, Tsc1 null astrocytes were not enlarged, and no spontaneous seizures were observed in studies carried out to 4 wk of age (49). These observations support our model that an extended period after recombination and loss of Tsc1/Tsc2 is required for giant cell development.

Similar to other TSC brain models (50, 51), rapamycin therapy was effective in this model, extending survival and extinguishing clinical manifestations of both hyperactivity and seizures. The fundamental understanding of the role of the *TSC1* and *TSC2* gene products in the regulation of the state of activation of the
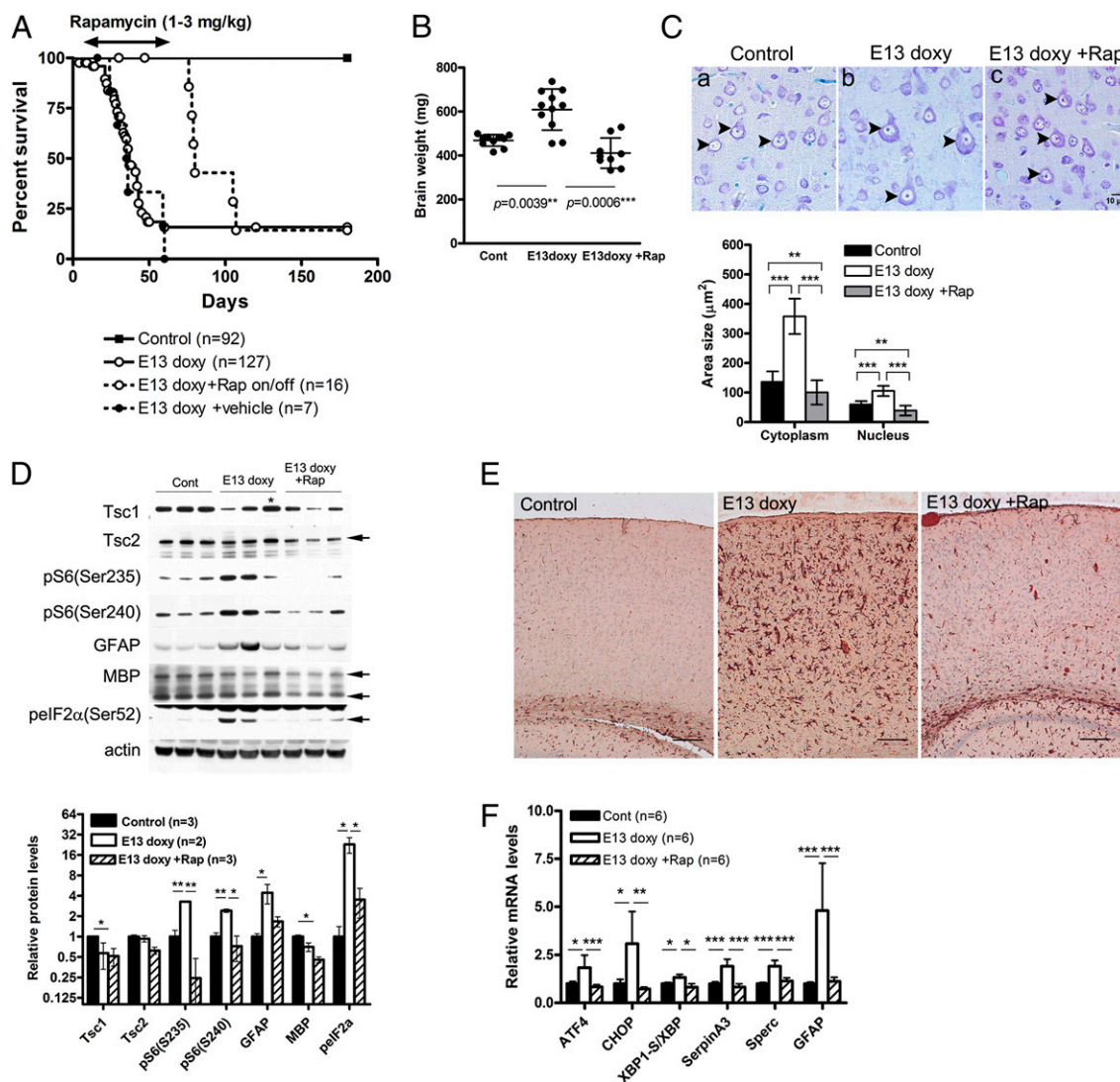
Fig. 7. Postnatal rapamycin treatment rescues survival and improves multiple aspects of the phenotype of *Tsc1^{cc} Nes-rtTA$^+$ TetOp-cre$^+$* (*E13 doxy*) mice. (*A*) Survival curves of *Tsc1^{cc} Nes-rtTA$^+$ TetOp-cre$^+$* (*E13 doxy*) mice treated with rapamycin from P8–P55 and then taken off the drug (Rap on/off). The survival of treated mutant mice at P55 is significantly different from that of both untreated (*P* = 0.0032) and vehicle-treated (*P* = 0.0022) mutants. After removal of rapamycin, the mutants started to die within 2 wk. (*B*) Brain weight of P30 animals. (*C*) (*Upper*) Cortical layer V pyramidal neurons (arrowheads) at P42. (Scale bar: 10 μm.) (*Lower*) Graph of neuronal area and neuronal nucleus area of pS6$^+$ cortical cells in control, mutant, and rapamycin-treated mutant mice. (*D*) Immunoblot analysis of rapamycin-treated mutants at P30 shows a reduction in mTORC1 activation markers, phospho-eIF2α, and GFAP levels. Only MBP levels remain low. An asterisk denotes a mutant with low or undetectable levels of *Tsc1* recombination. Quantitation of immunoblot band intensity is shown at the bottom. Cont, control. (*E*) IHC staining for GFAP on cortical sections from control, *E13 doxy* mutant, and *E13 doxy* mutant treated with rapamycin, all at P30 (*n* = 3). (Scale bars: 100 μm.) (*F*) Real-time qPCR analysis using hippocampal RNA of rapamycin-treated mutant (*n* = 6) at P30 shows that *ATF4, CHOP, SerpinA3, Sperc,* and *GFAP* levels returned to normal in response to rapamycin. Rapamycin was given i.p. for 3 d each week at a dose of 1 mg/kg for P8–P20 and 3 mg/kg for P21–P55. **P* < 0.05; ***P* < 0.01; ****P* < 0.001.

mTORC1 complex has led to recent renewed hope for patients with TSC and their families that drugs blocking this abnormal activation of mTORC1 in TSC lesions will improve clinical outcomes (2, 3). Indeed, rapamycin and a related compound, everolimus, have been shown to have major benefit in the treatment of the TSC brain tumor subependymal giant cell astrocytomas (52, 53). Although there is benefit, it appears that long-term treatment with drug is required to maintain response in many patients, and the effect of long-term and early neonatal rapamycin treatment on brain development and cognitive function has not yet been investigated (2). We initiated rapamycin therapy about 2 wk after induction of recombination with doxycycline, with an excellent overall response, suggesting that a 2-wk period without suppression of aberrant mTORC1 activation during late prenatal and early postnatal development did not have long-term major consequences. This suggests the pos-

sibility of benefit in the human situation, in which rapamycin therapy might be given months after cortical tuber formation during embryogenesis. However, reduced MBP levels seen in untreated mutants were not restored by rapamycin treatment, consistent with an inhibitory effect of early postnatal rapamycin treatment on oligodendrocyte maturation and myelination (54, 55) and/or incomplete reversal of all molecular pathology attributable to loss of *Tsc1*.

In summary, we have generated a model of TSC brain disease that replicates the key clinical and pathological features of TSC cortical tubers, as well as previously unappreciated characteristics of giant cells: vacuolation, abnormal dendritic morphology, and markedly increased mitochondria. The model provides evidence that biallelic mosaic inactivation is responsible for giant cell formation and enables further insight into new therapies for TSC neurological disease, including rapamycin and related drugs;

NEUROSCIENCE

benefit of epileptic treatment; and detailed analysis of the molecular pathogenesis of seizure development and other neurological deficits.

Materials and Methods

Mouse Procedures. Mouse experiments were performed in a mixed-strain background to accommodate the combination of alleles studied here. Mice bearing the *TetOp-Cre* (LC-1) and *Nes-rtTA* alleles were kindly provided by Robert Koesters (Universitaetsklinikum Heidelberg, Heidelberg, Germany) (30). Generation of *Tsc1^c* and *Rosa-26* alleles in mice has been described previously (28, 56). Mice were generated through breeding between *Tsc1^{cc} Nes-rtTA^{++}* females and either *Tsc1^{cc} TetOp-Cre^{++} Rosa-26^{++}* or *Tsc1^{cc} TetOp-Cre$^+$ Rosa-26^{++}* males. Timed matings were performed using the vaginal plug to assess fertilization. Chow containing doxycycline (2,000 ppm, test diet) was given to pregnant dams for 24 h on the embryonic day indicated. Routine mouse genotyping (28, 30) and MLPA analysis for checking zygosity of transgenes (57) were performed as indicated previously. All procedures were carried out in accordance with the Guide for the Humane Use and Care of Laboratory Animals, and the study was approved by the Animal Care and Use Committee of Children's Hospital Boston. Individual mice were euthanized when a weight loss of 20%, greatly reduced movement, or other signs of morbidity were seen.

Materials. Antibodies were obtained from the following sources: rabbit polyclonal antibodies to Tsc1 and rabbit monoclonal antibodies to pS6(Ser235/6) (no. 4857), pS6(Ser240/4) (no. 2215), and Tsc2 (no. 4308) from Cell Signaling Technology; rabbit polyclonal antibodies to MBP, goat polyclonal antibody to Akt, rat monoclonal antibody to LAMP1, mouse monoclonal antibody to HuD, rabbit polyclonal antibody to NR2D, and rabbit polyclonal antibody to GFP as well as HRP-labeled anti-mouse, anti-goat, and anti-rabbit secondary antibodies from Santa Cruz Biotechnology; rabbit monoclonal antibody to pAkt(Ser473) from Dako; mouse monoclonal antibody to actin from Sigma; mouse monoclonal antibody to EEA1 from BD Bioscience; rabbit polyclonal antibody to phospho-eIF2α(Ser52) and Alexa 488- or Alexa 594-labeled secondary antibody from Invitrogen; rabbit polyclonal antibody to Rab7 from Abcam; rabbit polyclonal antibody to Grp78 from Stressgen; and mouse monoclonal antibody to GFAP, mouse monoclonal NeuN antibody, and rabbit polyclonal antibody to GluR4 from Millipore.

EEG and Video Monitoring. Control and mutant mice aged P24–P40 (n = 26) were implanted with three-channel epidural screw electrodes (Plastics One) to monitor cortical EEG activity. The electrodes were placed under general anesthesia using pentobarbital (62.5 mg/kg administered i.p.). Two electrodes were placed over each cerebral hemisphere ~1.5 mm lateral from the midline and 2 mm posterior from bregma, with the third reference electrode placed about 1 mm anterior to bregma, either 0.5 mm right or left from the midline to allow bipolar, epidural, continuous EEG recordings. The electrodes were placed in 1-mm-diameter holes drilled in the skull and were lowered until firmly secured yet not penetrating the dura before being anchored to the skull with dental cement.

High-quality video-EEG recording was performed using a digital Harmonie Video EEG acquisition system (Stellate Systems, Inc.). Continuous video-EEG monitoring started 1–7 d postsurgery, with recording sessions usually lasting between 16 h and 41 h (24 of 26 mice). Most mice (19 of 26) were repeatedly monitored over several weeks. The skull was carefully inspected during and after recordings, as well as the brain when animals were killed, to exclude brain injury effects attributable to electrode placement. Entire EEG recording sessions were reviewed for abnormal interictal activity (spikes, high-amplitude sharp waves, and spike-suppression pattern) and spontaneous seizures (epileptiform discharges lasting >10 s). The average frequency (number of seizures per day) and seizure duration were evaluated for each animal, and the behavioral correlate was examined by inspection of simultaneous video recordings.

Histology, IHC, and Fluorescent Microscopy. Standard histology sections of mouse brains were prepared after euthanasia with CO_2 and 2–4 d of fixation with Bouin's solution (Sigma). Following paraffin embedding, 5-μm sections were cut and stained with either H&E, Luxol fast blue, Nissl, or Bielschowsky silver stain or were used for IHC. IHC was performed after deparaffinization and rehydration steps and antigen retrieval in citrate buffer (pH 6) using the Envision system (DAKO) or HistoMouse-Plus kit (Invitrogen). For immunofluorescence microscopy, mice were perfused with and fixed overnight in 4% (wt/vol) paraformaldehyde (PFA) in PBS at 4 °C and brains were cryoprotected in 30% (wt/vol) sucrose at 4 °C overnight. Coronal brain sections (12–50 μm) were cut with a cryostat and stained as described previously (49).

LacZ staining was performed on 20-μm frozen brain sections as described previously (28). Golgi staining was performed using an FD Rapid Golgistain kit (FD NeuroTechnologies) following the manufacturer's instructions.

Cell Size Analysis. Cortical brain sections, including somatosensory cortex, for each of at least two matched mice in each cohort were stained with either pS6 (S235) antibody or Nissl staining. Images were examined using National Institutes of Health ImageJ software v1.31 to calculate cell size (μm^2) after manual drawing of cell margins. All cells in a field with a magnification of 40× were measured, independent of pS6 staining, for a minimum of eight cells per field. The largest three cells per field were included in the formal measurements for statistical comparison using the t test.

Sholl Analysis. Thick (100 μm) coronal Golgi-stained brain sections, including anterior hippocampus, of control (n = 3) and mutant (n = 3) animals were viewed on a Leica DMR microscope operated by Neurolucida (MBF Bioscience). Eight to nine typical pyramidal neurons from either layer V or layer VI in hind limb and forelimb sensorimotor cortex were individually traced and reconstructed as 3D images on Neurolucida. The number of basal dendrites crossing sequential circles (radius of 10–250 μm) starting at the cell body was counted using NeuroExplorer (Nex Technologies). The Student t test was applied to all data points individually.

EM. For transmission EM images, mice were perfused with 2.5% (vol/vol) glutaraldehyde, 1.25% (wt/vol) PFA, and 0.03% picric acid in 0.1 M sodium cacodylate buffer (pH 7.4). Small pieces (1- to 2-mm cubes) of brain were processed and embedded in TAAB Epon (Marivac Canada, Inc.). The following day, the samples were embedded in TAAB Epon and polymerized at 60 °C for 48 h. Ultrathin sections (90 nm) were cut on a Reichert Ultracut-S microtome, picked up onto copper grids, stained with lead citrate, and examined in a JEOL 1200EX transmission electron microscope. Images were recorded with an AMT 2k CCD camera (Advanced Microscopy Techniques, Woburn, MA). For immuno-EM microscopy, mice were perfused with 3.57% (vol/vol) acrolein and 2% (wt/vol) PFA in PBS and brains were postfixed overnight at 4 °C. Brains were kept at 4 °C in 0.2% PFA in PBS before they were cut into 50-μm sections with a vibratome. Brain slices were incubated in 1% sodium borohydride in PBS for 30 min, washed three times in PBS, and rinsed in Tris-buffered saline (TBS). After the overnight incubation in each primary antibody, and following three washes in TBS, the sections were placed on 0.2% gelatin-PBS in 0.8% BSA for 5 min and then incubated in goat–anti-rabbit IgG bound to 1.4-nm colloidal gold (Nanoprobes) for 2 h. The sections were then washed three times in PBS, fixed in 1% glutaraldehyde in PBS for 10 min, and washed three times in water, followed by a rinse with 0.02 M sodium citrate buffer (pH 7.4). Silver enhancement with HQSilver (HQ silver Enhancement kit, no. 2012; Nanoprobes) was carried out for 6 min at room temperature in the dark. The sections were then rinsed in water three times and incubated in 0.5% osmium tetroxide for 30 min, followed by dehydration and embedding in TAAB Epon as above.

Western Blotting, qPCR, and MLPA Analysis. Animals were euthanized with CO_2, and brains were rapidly removed, dissected, and flash-frozen in liquid N_2. Total tissue lysates for Western blotting were prepared and analyzed as described previously (28). Densitometry was performed to permit quantitative analysis of chemiluminescent bands seen by Western blotting using ImageJ software. The relative expression level of each protein was normalized to β-actin, and the average of several samples was compared with the average of WT controls.

Total hippocampal RNA from P30 mice for qPCR was isolated using an RNAeasy mini kit (Qiagen) following the manufacturer's protocol. After the quality check using a nanodrop device, cDNAs were synthesized with oligo-dT20 primers and SuperScript 3 (Invitrogen). Total brain DNAs, including gDNA and mtDNA, were isolated using a Gentra Puregene Tissue kit (Qiagen). qPCR analysis was performed with primers for genes in the ER stress pathway (25), and genes were shown to be up-regulated in some tuber samples from patients with TSC (41). Real-time qPCR was performed with SYBR green containing PCR master mix (Quanta) using an ABI 9700 Thermal Cycler (Applied Biosystems). Quantity of RNA expression levels was normalized to 36b4 mRNA levels. The average quantity of mtDNA assessed using primers for NADH dehydrogenase, J01420, and cytochrome *b* was normalized to gDNA contents. For MLPA analysis, gDNA from P0 brains was isolated using a DNA isolation kit (Qiagen). MLPA analysis to determine the gene recombination ratio at the *Tsc1^c* allele was performed as indicated previously (58).

Rapamycin Treatment. Rapamycin (R-5000; LC Laboratories), dissolved in sterile vehicle containing 0.25% Tween 80 and 0.25% PEG, was given by i.p. injection to P8–P20 mice at a dose of 1 mg/kg for 3 d each week and to P21 or older mice at a dose of 3 mg/kg for 3 d each week.

Human Cortical Tuber Specimens. Cortical tubers were removed from pediatric patients with TSC for seizure control. They were fixed in formalin for several days following standard methods, and paraffin slides were prepared for H&E and routine IHC. This study was approved by the Institutional Review Board for the Partners Hospitals.

1. Jozwiak J, Jozwiak S, Wlodarski P (2008) Possible mechanisms of disease development in tuberous sclerosis. *Lancet Oncol* 9(1):73–79.
2. Kwiatkowski DJ, Thiele EA, Whittemore VH, eds (2010) *Tuberous Sclerosis Complex: Genes, Clinical Features, and Therapeutics* (Wiley–VCH, Weinheim, Germany), p 432.
3. Thiele EA (2004) Managing epilepsy in tuberous sclerosis complex. *J Child Neurol* 19:680–686.
4. Holmes GL, Stafstrom CE; Tuberous Sclerosis Study Group (2007) Tuberous sclerosis complex and epilepsy: Recent developments and future challenges. *Epilepsia* 48:617–630.
5. Doherty C, Goh S, Young Poussaint T, Erdag N, Thiele EA (2005) Prognostic significance of tuber count and location in tuberous sclerosis complex. *J Child Neurol* 20:837–841.
6. Winterkorn EB, Pulsifer MB, Thiele EA (2007) Cognitive prognosis of patients with tuberous sclerosis complex. *Neurology* 68:62–64.
7. Yamanouchi H, Jay V, Rutka JT, Takashima S, Becker LE (1997) Evidence of abnormal differentiation in giant cells of tuberous sclerosis. *Pediatr Neurol* 17(1):49–53.
8. Crino PB, Trojanowski JQ, Dichter MA, Eberwine J (1996) Embryonic neuronal markers in tuberous sclerosis: Single-cell molecular pathology. *Proc Natl Acad Sci USA* 93:14152–14157.
9. Talos DM, Kwiatkowski DJ, Cordero K, Black PM, Jensen FE (2008) Cell-specific alterations of glutamate receptor expression in tuberous sclerosis complex cortical tubers. *Ann Neurol* 63:454–465.
10. Jozwiak J, Jozwiak S (2007) Giant cells: Contradiction to two-hit model of tuber formation? *Cell Mol Neurobiol* 27:251–261.
11. Huttenlocher PR, Wollmann RL (1991) Cellular neuropathology of tuberous sclerosis. *Ann N Y Acad Sci* 615(1):140–148.
12. Bordarier C, Lellouch-Tubiana A, Robain O (1994) Cardiac rhabdomyoma and tuberous sclerosis in three fetuses: A neuropathological study. *Brain Dev* 16:467–471.
13. Park SH, et al. (1997) Tuberous sclerosis in a 20-week gestation fetus: Immuno-histochemical study. *Acta Neuropathol* 94(2):180–186.
14. Wei JJ, et al. (2002) Tuberous sclerosis in a 19-week fetus: Immunohistochemical and molecular study of hamartin and tuberin. *Pediatr Dev Pathol* 5:448–464.
15. van Slegtenhorst M, et al. (1997) Identification of the tuberous sclerosis gene TSC1 on chromosome 9q34. *Science* 277:805–808.
16. Nellist M, et al.; European Chromosome 16 Tuberous Sclerosis Consortium (1993) Identification and characterization of the tuberous sclerosis gene on chromosome 16. *Cell* 75:1305–1315.
17. Sabatini DM (2006) mTOR and cancer: Insights into a complex relationship. *Nat Rev Cancer* 6:729–734.
18. Fingar DC, Blenis J (2004) Target of rapamycin (TOR): An integrator of nutrient and growth factor signals and coordinator of cell growth and cell cycle progression. *Oncogene* 23:3151–3171.
19. Laplante M, Sabatini DM (2009) An emerging role of mTOR in lipid biosynthesis. *Curr Biol* 19:R1046–R1052.
20. Porstmann T, et al. (2008) SREBP activity is regulated by mTORC1 and contributes to Akt-dependent cell growth. *Cell Metab* 8:224–236.
21. Ma XM, Blenis J (2009) Molecular mechanisms of mTOR-mediated translational control. *Nat Rev Mol Cell Biol* 10:307–318.
22. Cunningham JT, et al. (2007) mTOR controls mitochondrial oxidative function through a YY1-PGC-1alpha transcriptional complex. *Nature* 450:736–740.
23. Jung CH, Ro SH, Cao J, Otto NM, Kim DH (2010) mTOR regulation of autophagy. *FEBS Lett* 584:1287–1295.
24. Ozcan U, et al. (2008) Loss of the tuberous sclerosis complex tumor suppressors triggers the unfolded protein response to regulate insulin signaling and apoptosis. *Mol Cell* 29:541–551.
25. Di Nardo A, et al. (2009) Tuberous sclerosis complex activity is required to control neuronal stress responses in an mTOR-dependent manner. *J Neurosci* 29:5926–5937.
26. Finlay GA, Thannickal VJ, Fanburg BL, Kwiatkowski DJ (2005) Platelet-derived growth factor-induced p42/44 mitogen-activated protein kinase activation and cellular growth is mediated by reactive oxygen species in the absence of TSC2/tuberin. *Cancer Res* 65:10881–10890.
27. Uhlmann EJ, et al. (2002) Astrocyte-specific TSC1 conditional knockout mice exhibit abnormal neuronal organization and seizures. *Ann Neurol* 52:285–296.
28. Meikle L, et al. (2007) A mouse model of tuberous sclerosis:Neuronal loss of Tsc1 causes dysplastic and ectopic neurons, reduced myelination, seizure activity, and limited survival. *J Neurosci* 27:5546–5558.
29. Way SW, et al. (2009) Loss of Tsc2 in radial glia models the brain pathology of tuberous sclerosis complex in the mouse. *Hum Mol Genet* 18:1252–1265.
30. Yu TS, Dandekar M, Monteggia LM, Parada LF, Kernie SG (2005) Temporally regulated expression of Cre recombinase in neural stem cells. *Genesis* 41(4):147–153.
31. Anderl S, Freeland M, Kwiatkowski DJ, Goto J (2011) Therapeutic value of prenatal rapamycin treatment in a mouse brain model of tuberous sclerosis complex. *Hum Mol Genet*, 10.1093/hmg/ddr393.
32. Ikenoue T, Inoki K, Yang Q, Zhou X, Guan KL (2008) Essential function of TORC2 in PKC and Akt turn motif phosphorylation, maturation and signalling. *EMBO J* 27:1919–1931.
33. Facchinetti V, et al. (2008) The mammalian target of rapamycin complex 2 controls folding and stability of Akt and protein kinase C. *EMBO J* 27:1932–1943.
34. Blümcke I, et al. (2011) The clinicopathologic spectrum of focal cortical dysplasias: A consensus classification proposed by an ad hoc Task Force of the ILAE Diagnostic Methods Commission. *Epilepsia* 52:158–174.
35. Choi Y, et al. (2008) Tuberous sclerosis complex proteins control axon formation. *Genes Dev* 22:2485–2495.
36. Chow DK, et al. (2009) Laminar and compartmental regulation of dendritic growth in mature cortex. *Nat Neurosci* 12(2):116–118.
37. Kwon CH, et al. (2006) Pten regulates neuronal arborization and social interaction in mice. *Neuron* 50:377–388.
38. Kimball SR, Fabian JR, Pavitt GD, Hinnebusch AG, Jefferson LS (1998) Regulation of guanine nucleotide exchange through phosphorylation of eukaryotic initiation factor eIF2alpha. Role of the alpha- and delta-subunits of eiF2b. *J Biol Chem* 273:12841–12845.
39. Harding HP, Zhang YH, Ron D (1999) Protein translation and folding are coupled by an endoplasmic-reticulum-resident kinase. *Nature* 397:271–274.
40. Kaufman RJ (1999) Stress signaling from the lumen of the endoplasmic reticulum: Coordination of gene transcriptional and translational controls. *Genes Dev* 13:1211–1233.
41. Boer K, et al. (2010) Gene expression analysis of tuberous sclerosis complex cortical tubers reveals increased expression of adhesion and inflammatory factors. *Brain Pathol* 20:704–719.
42. Sancak Y, et al. (2008) The Rag GTPases bind raptor and mediate amino acid signaling to mTORC1. *Science* 320:1496–1501.
43. Sancak Y, et al. (2010) Ragulator-Rag complex targets mTORC1 to the lysosomal surface and is necessary for its activation by amino acids. *Cell* 141:290–303.
44. Yu L, et al. (2010) Termination of autophagy and reformation of lysosomes regulated by mTOR. *Nature* 465:942–946.
45. Wong M, et al. (2003) Impaired glial glutamate transport in a mouse tuberous sclerosis epilepsy model. *Ann Neurol* 54:251–256.
46. Zeng LH, Bero AW, Zhang B, Holtzman DM, Wong M (2010) Modulation of astrocyte glutamate transporters decreases seizures in a mouse model of Tuberous Sclerosis Complex. *Neurobiol Dis* 37:764–771.
47. Crino PB, Aronica E, Baltuch G, Nathanson KL (2010) Biallelic TSC gene inactivation in tuberous sclerosis complex. *Neurology* 74:1716–1723.
48. Mizuguchi M, Kato M, Yamanouchi H, Ikeda K, Takashima S (1996) Loss of tuberin from cerebral tissues with tuberous sclerosis and astrocytoma. *Ann Neurol* 40:941–944.
49. Feliciano DM, Su T, Lopez J, Platel JC, Bordey A (2011) Single-cell Tsc1 knockout during corticogenesis generates tuber-like lesions and reduces seizure threshold in mice. *J Clin Invest* 121:1596–1607.
50. Meikle L, et al. (2008) Response of a neuronal model of tuberous sclerosis to mammalian target of rapamycin (mTOR) inhibitors: Effects on mTORC1 and Akt signaling lead to improved survival and function. *J Neurosci* 28:5422–5432.
51. Zeng LH, Xu L, Gutmann DH, Wong M (2008) Rapamycin prevents epilepsy in a mouse model of tuberous sclerosis complex. *Ann Neurol* 63:444–453.
52. Lam C, et al. (2010) Rapamycin (sirolimus) in tuberous sclerosis associated pediatric central nervous system tumors. *Pediatr Blood Cancer* 54:476–479.
53. Krueger DA, et al. (2010) Everolimus for subependymal giant-cell astrocytomas in tuberous sclerosis. *N Engl J Med* 363:1801–1811.
54. Tyler WA, et al. (2009) Activation of the mammalian target of rapamycin (mTOR) is essential for oligodendrocyte differentiation. *J Neurosci* 29:6367–6378.
55. Narayanan SP, Flores AI, Wang F, Macklin WB (2009) Akt signals through the mammalian target of rapamycin pathway to regulate CNS myelination. *J Neurosci* 29:6860–6870.
56. Mao XH, Fujiwara Y, Orkin SH (1999) Improved reporter strain for monitoring Cre recombinase-mediated DNA excisions in mice. *Proc Natl Acad Sci USA* 96:5037–5042.
57. Kozlowski P, Lin M, Meikle L, Kwiatkowski DJ (2007) Robust method for distinguishing heterozygous from homozygous transgenic alleles by multiplex ligation-dependent probe assay. *Biotechniques*, 42:584, 586, 588.
58. Liang MC, et al. (2010) TSC1 loss synergizes with KRAS activation in lung cancer development in the mouse and confers rapamycin sensitivity. *Oncogene* 29:1588–1597.

PNAS PLUS

NEUROSCIENCE